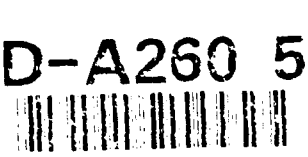

College of Earth and Mineral Sciences

PENNSTATE

ANNUAL REPORT

to

OFFICE OF NAVAL RESEARCH

Contract USN 00014--91-J-1189

January 1993

PREDICTION OF HYDROGEN ENTRY AND PERMEATION IN METALS AND ALLOYS

H. W. Pickering

Department of Materials Science and Engineering
The Pennsylvania State University

PENN STATE
College of Earth and Mineral Sciences

Undergraduate Majors

Ceramic Science and Engineering, Fuel Science, Metals Science and Engineering, Polymer Science; Mineral Economics; Mining Engineering, Petroleum and Natural Gas Engineering; Earth Sciences, Geosciences; Geography; Meteorology.

Graduate Programs and Fields of Research

Ceramic Science and Engineering, Fuel Science, Metals Science and Engineering, Polymer Science; Mineral Economics; Mining Engineering, Mineral Processing, Petroleum and Natural Gas Engineering;
Geochemistry and Mineralogy, Geology, Geophysics; Geography; Meteorology.

Universitywide Interdisciplinary Graduate Programs Involving EMS Faculty and Students

Earth Sciences, Ecology, Environmental Pollution Control Engineering, Mineral Engineering Management, Solid State Science.

Associate Degree Programs

Metallurgical Engineering Technology (Shenango Valley Campus).

Interdisciplinary Research Groups Centered in the College

C. Drew Stahl Center for Advanced Oil Recovery, Center for Advanced Materials, Coal Research Section, Earth System Science Center, Mining and Mineral Resources Research Institute, Ore Deposits Research Group.

Analytical and Characterization Laboratories (Mineral Constitution Laboratories)

Services available include: classical chemical analysis of metals and silicate and carbonate rocks; X-ray diffraction and fluorescence; electron microscopy and diffraction; electron microprobe analysis; atomic absorption analysis; spectrochemical analysis; surface analysis by secondary ion mass spectrometry (SIMS); and scanning electron microscopy (SEM).

U Ed 87-1027
Produced by the Penn State Department of Publications

REPORT DOCUMENTATION PAGE

Form Approved
OMB No. 0704-0188

1. AGENCY USE ONLY (*Leave blank*)	2. REPORT DATE	3. REPORT TYPE AND DATES COVERED
	January 1993	Annual 10/1/91 to 9/30/92

4. TITLE AND SUBTITLE
Prediction of Hydrogen Entry and Permeation in Metals and Alloys

5. FUNDING NUMBERS
N00014-91-J-1189
431 5098

6. AUTHOR(S)
Howard W. Pickering

7. PERFORMING ORGANIZATION NAME(S) AND ADDRESS(ES)
The Pennsylvania State University
Department of Materials Science and Engineering
326 Steidle Building
University Park, PA 16802

8. PERFORMING ORGANIZATION REPORT NUMBER

9. SPONSORING/MONITORING AGENCY NAME(S) AND ADDRESS(ES)
Scientific Officer
Materials Division Code: 1131M
Office of Naval Research
Arlington VA 22217-5000
ATTN: A. John Sedricks

10. SPONSORING/MONITORING AGENCY REPORT NUMBER

11. SUPPLEMENTARY NOTES

12a. DISTRIBUTION/AVAILABILITY STATEMENT
Approved for public release; distribution is unlimited.

12b. DISTRIBUTION CODE

13. ABSTRACT (*Maximum 200 words*)

This report summarizes results of the past year on our continuing experiments directed to the problem of hydrogen entry and degradation of materials both of planar surfaces and for the more complicated recessed surface. For the planar surface the hydrogen permeation and scanning tunneling microscopy (STM) techniques are being used, and for the recessed surface the study uses the hydrogen permeation technique and a microscopy/electrochemical probe technique.

In-situ scanning tunneling microscopy (STM) of hydrogen adsorption from the gas phase on Si 111(7x7) demonstrates the feasibility of STM for atomic scale study of adsorbed hydrogen. In aqueous solutions both acidification and chloride ion accumulation within recesses in iron surfaces cause enhanced proton reduction and hydrogen absorption. Flat, smooth surfaces can form or develop recesses as a result of corrosion or other reasons, e.g., grain boundary grooves that form during corrosion of Cr-depleted alloy in sensitized stainless steel. These recesses are found to be just as prone to proton discharge and hydrogen absorption as pre-existing recesses.

14. SUBJECT TERMS	15. NUMBER OF PAGES
KEY WORDS: scanning tunneling microscopy, hydrogen permeation cell, hydrogen absorption, chloride ion and acidification effects, hydrogen evolution in recesses, corrosion-produced recesses, grain boundary grooves.	16. PRICE CODE

17. SECURITY CLASSIFICATION OF REPORT	18. SECURITY CLASSIFICATION OF THIS PAGE	19. SECURITY CLASSIFICATION OF ABSTRACT	20. LIMITATION OF ABSTRACT
UNCLASSIFIED	UNCLASSIFIED	UNCLASSIFIED	

CONTENTS

REPORT DOCUMENTATION PAGE.....

INTRODUCTION .....

SECTION 1: PROGRESS SUMMARY.....

HYDROGEN ABSORPTION.....

IN-SITU IMAGING OF HYDROGEN ADSORPTION.....

PROTON REDUCTION AND HYDROGEN ABSORPTION WITHIN RECESSES .....

PUBLICATIONS .....

SECTION 2: HYDROGEN ABSORPTION IN GRAIN BOUNDARY GROOVES.....

SECTION 3: PREVIOUSLY OBTAINED RESULTS FOR SENSITIZED STAINLESS STEEL RELEVANT TO SECTION 2 .....

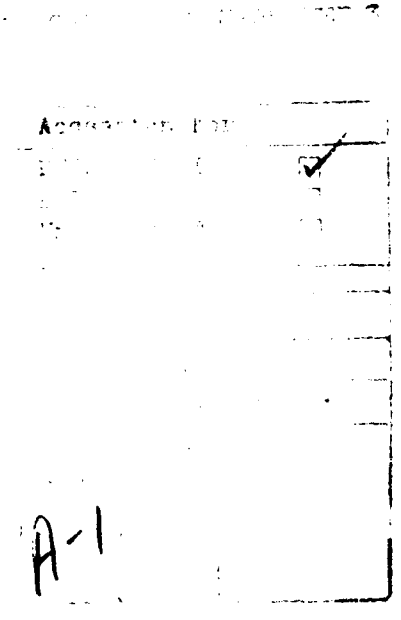

A-1

INTRODUCTION

This report is divided into three sections. Section 1 is a summary of progress and a list of project publications in the past year. Section 2 is a report of hydrogen permeation data showing on hydrogen absorption (entry) from within grain boundary grooves during anodic dissolution of the sample. The results illustrate the importance of the IR voltage drop in the groove on creating the conditions for proton reduction and the subsequent entry of atomic hydrogen into the metal. They also confirm the conclusion of an earlier ONR study (USN 00014-8-K-0025) that grain boundary corrosion can sustained indefinitely once a grain boundary groove is produced. Section 3 describes results from this earlier study where the groove was produced by the classical chromium depletion mechanism followed by rapid localized corrosion of the adjacent (18% Cr) bulk grains

SECTION 1

PROGRESS SUMMARY

Hydrogen Absorption. The problem of hydrogen-induced damage and failure of metallic systems starts with hydrogen entry. The hydrogen permeation technique has been successfully used for three decades for determining some of the important hydrogen/material parameters, e.g., the hydrogen diffusivity and hydrogen concentration inside the input surface, but most of the parameters related to hydrogen entry were not previously attainable from permeation data because of the incomplete nature of the quantitative treatment of hydrogen permeation available in the literature. Our work of the past few years on the project corrected this situation for aqueous solution hydrogen charging, so now a more rigorous quantitative treatment of the permeation process is available (described in the 1990 Annual Report and various publications). As a result several additional parameters related to hydrogen entry became attainable from steady stage permeation data obtained as a function of the hydrogen charging current and in some cases the membrane thickness. The model shows how the proton discharge rate constant, transfer coefficient and exchange current density, the hydrogen recombination rate constant, the hydrogen coverage, and the ratio of (but not the individual) hydrogen absorption and desorption rate

constants can be obtained from data for a single membrane thickness. To obtain the individual absorption and desorption constants further development of the model (described in the 1992 Annual Report and publications) shows how these parameters are obtained from steady state permeation data for three or more membrane thicknesses. Application of the model to hydrogen permeation data is underway or anticipated in order to better understand the effects of a number of metallurgical and environmental factors on which are known to modify hydrogen absorption characteristics and kinetics.

In-situ imaging of hydrogen adsorption at the atomic level. The scanning tunneling microscope provides the opportunity for in-situ imaging of the surface over a wide range of scale including the atomic scale. Imaging adsorbates on surfaces including hydrogen from the gas phase is also possible. Our in-situ STM observations of hydrogen adsorption for the Si 111(7x7) surface (ONR Technical Report, February 1990) demonstrate the applicability of the technique for atomic scale study of adsorbed hydrogen. Recent progress is reported in ONR Technical Report, February 1993 entitled "FI-STM Investigation of Atomic Hydrogen Adsorption on the Si(100) 2x1 Surface". Many details of the atomic surface structure and how the hydrogen chemisorption structure changes as a function of external factors such as the hydrogen pressure and time (coverage).

Proton reduction and hydrogen absorption within recesses. For most cases of nonuniform corrosion, the electrode potential varies over the surface, e.g., in the case of oxygen concentration cells, being me noble at cathodic sites of high oxidant availability and more negative at anodic sites. The shift of the electrode potential in the negative direction can be quite large and its magnitude is unknown in service applications since the anodic sites are in recesses (crevice, cracks, etc.). It follows that the tendency for the occurrence of the hydrogen evolution reaction, and thus for hydrogen entry into the metal structure, is greatest in the recesses.

Thus, it becomes important to know how and to what extent the various parameters e.g., size and shape of the cavity, shift the local electrode potential in the negative direction during localized corrosion. This question does not appear to have been addressed in the literature but is not trivial

as we now know from recent results on IR voltage drops in cavities. These IR voltages produce electrode potential shifts that can evolve hydrogen gas (ONR Technical Reports, February 1988, January 1988 and October 1987, and Annual Report 1992; J. Electrochem. Soc., 137, 3313 (1990); ibid, 138, L56 (1991). Our recent results show both acidification and chloride ion increase the magnitude and frequency of the potential shift within recesses in the negative direction, favoring hydrogen evolution and entry into the metal, and earlier results show that flat surfaces may form grooves by one corrosion process, e.g., grain boundary attack of Cr-depleted alloy in sensitized stainless steel (described below in Section 3) that are amenable to IR-induced proton discharge and hydrogen absorption (described below in Section 2).

PUBLICATIONS ON THE PROJECT

K. Cho and H. W. Pickering, "The Role of Chloride Ions in the IR>IR* Criterion for Crevice Corrosion in Iron", Extended Abs., Electrochem. Soc., Vol. 91-2, Pennington, NJ, 1991; ibid J. Electrochem. Soc., 138, L56-L58 (1991).

K. Cho and H. W. Pickering, "The Role of Chloride Ions in the IR>IR* Criterion for Crevice Corrosion in Iron", pp. 407-419 in Proc. Sym. on Critical Factors in Localized Corrosion, Electrochem. Soc., Pennington, NJ (1992).

Yuan Xu and H. W. Pickering, "The Initial Potential Current Distributions of the Crevice Corrosion Process", J. Electrochem. Soc., 140 (March, 1993).

X. D. Wang, T. Hashizume, H. Lu, H. W. Pickering and T. Sakurai, "FI-STM Investigation of Atomic Hydrogen Adsorption on the Si(100)2X1 Surface", Phy. Rev. B., (1992), in press.

H. W. Pickering, K. Cho and E. Nystrom, "A Microscopy/Local Probe Method for Studying Crevice Corrosion and Its Application to Iron and Stainless Steel", Advances in Corrosion and Protection, UMIST (June 28, 1992, Manchester, England), Corrosion Sci., in press.

X. Wang, H. Lu, T. Hashizume, H. W. Pickering and T. Sakurai, "Atomic Hydrogen Chemisorption on Si(200) 2X1 Studied by FI-STM", (39th Intern. Field Emission Sym., Dalhousie University, Newfoundland, August 10-14, 1992), Appl. Surf. Sci., in press.

H. W. Pickering, "On the Mechanism of Crevice Corrosion and Its Consequences for Crack Initiation", pp. . in Directions for Research on Corrosion-Assisted Crack Initiate (EPRI Workshop, Chicago, IL, September 23-25, 1992), in press.

Yong Xu and H. W. Pickering, "A New Index for the Crevice Corrosion Resistance of Materials", Accelerated Corrosion Tests to Service Life Prediction of Materials, ASTM, STP 1194, G. Cragolino and N. Sridhar, eds., American Society for Testing and Materials, Philadelphia, 1992.

SECTION 2

HYDROGEN ABSORPTION AT GRAIN BOUNDARIES DURING ANODIC POLARIZATION OF SENSITIZED STAINLESS STEEL BY THE HYDROGEN PERMEATION TECHNIQUE

A. Sehgal, R. N. Iyer, and H. W. Pickering

The Pennsylvania State University
Materials Science and Engineering Department
326 Steidle Building
University Park, PA 16802

ABSTRACT

Hydrogen permeation results are used to indirectly determine the electrode potential inside grain boundary grooves. The results indicate that the IR form of localized corrosion replaces the chromium depletion mechanism within minutes after grain boundary grooves form in a sensitized ferritic stainless steel. This results in rapid attack of the bulk stainless steel grains of normal Cr content.

INTRODUCTION

Intergranular corrosion (IGC) in stainless steels occurs primarily as a result of the formation of a chromium depleted zone at the grain boundary which forms a less protective passive film and is preferentially attacked. However, previous work on the project by Bennett and Pickering[1], and Kelly, et. al.[2] has shown that the grooves formed during IGC in an austenitic and ferritic steel, respectively, were much larger than the Cr depleted zone width. The same has been observed in a stainless steel tube that failed in service due to IGC in acid solution by Zamanzadeh, et.al.[3] Thus, in all three cases the bulk alloy, which should have been passive, was attacked, a result not explained by the chromium depletion theory. Therefore, a second corrosion form was indicated to occur and to dominate after initiation of IGC by the classical chromium depletion form of corrosion. Kelly also observed that the bulk of the attack was consistently subsurface, i.e., the majority of the IGC attack occurred inside the material and the widest part of the groove was below the specimen surface. Gas bubbles, deduced to be hydrogen, were also observed to be evolving from the grain boundary grooves, a notable result since the external surface was anodically

polarized into the passive region of the steel and therefore was far more noble then the equilibrium potential of the hydrogen evolution reaction (h.e.r.). If the gas was indeed hydrogen, it meant that hydrogen absorption into the steel and hydrogen embrittlement could occur under corrosion conditions for which the h.e.r. was not thermodynamically possible at the outer surface. It would also establish that there existed a sizable voltage (IR) drop within the grain boundary groove, i.e., sufficient in size to place the local electrode potential at the bottom of the groove in the active loop region of the alloy in the Kelly experiments. Thus, the corrosion mechanism that commences in a matter of minutes, replaces the Cr-depletion mechanism and accounts for the vast majority of IGC. It occurs following formation of the groove by the Cr-depletion corrosion mechanism, and may be the IR voltage drop mechanism of corrosion recently discovered to be responsible for crevice corrosion in iron and stainless steel* However, the evidence that this is the second form of corrosion observed by Bennett and Pickering[1] and Kelly et.al.,[2] rests on the assumption that the observed gas is hydrogen, albeit an assumption that is supported on thermodynamic grounds as the only gas that can form from water for the experimental conditions (corrosion or applied potential in the passive region below the oxygen reversible potential).

One way to prove that the gas is hydrogen is to detect it at the opposite surface of a sheet sample. This identification procedure relies on the fact that only hydrogen of all the elements can diffuse through a mm thick ferritic steel in minutes at 25°C. This fact is the basis for the hydrogen permeation technique[13] used widely for studying hydrogen entry and embrittlement of steels and other body centered cubic metals. At a cathodic potential, hydrogen ions in an aqueous solution will be reduced, resulting in hydrogen evolution, absorption (entry) of atomic hydrogen into the

---

* At the time of Kelly's work in the mid eighties, other investigations in our laboratory by Valdes[4-6] of crevice corrosion in iron were strongly hinting of a new, important phenomena in crevice corrosion, namely, a shift of the electrode potential inside the crevice in the negative direction to values outside the range of stable passivity. This shift in potential was caused by the IR voltage drop between the actively dissolving crevice wall and the passive outer surface. The IR voltage drop mechanism of crevice corrosion is now documented in the literature, and to date, has been shown to operate for a wide range of operating conditions of crevice corrosion in iron.[7-9] In principle, it is likely to operate in all forms of localized corrosion and in all metals exhibiting the passive state, since it has been observed to be a requirement for localized corrosion in every test conducted to date, which includes pit growth experiments and other metals like Ni[10] and stainless steel.[8] Localized corrosion that occurs by the IR mechanism is based on simple potential theory and is therefore, predictive as is shown already by application of the initial modeling work of Xu and Pickering[11,12] to experimental results.

alloy and permeation as shown in Figure 1a. Since, no other elements have such a high diffusivity as hydrogen, detection of an oxidation current at the exit surface in the permeation experiment depicted in Fig 1a is a proof that proton discharge occurred at the input surface.

If anodic, instead of cathodic, polarization is used in the left side in Fig. 1a, the h.e.r. will not occur. Only if a preexisting crevice is present or one is formed, e.g., along the grain boundary as is Fig. 1b, is it, in principle, possible for the h.e.r. to occur with the outer surface potential positive of the hydrogen equilibrium potential. So, if the entry of hydrogen into the steel undergoing IGC (Fig. 1b) can be proved by measurement of an oxidation current at the exit surface, it will establish that the electrode potential inside the grain boundary grooves is well negative of the surface value and in the region of the h.e.r. For base metals like steel, this means the potential is also in the vicinity of the anodic loop where large anodic currents are possible, Fig. 1c. In this work an electrochemical permeation technique[13] is employed using a thin membrane of a sensitized ferritic stainless steel (Type 430 stainless steel), to determine if the gas coming out of the grain boundary grooves is hydrogen.

The polarization curve of Type 430 stainless steel often shows a secondary anodic loop or secondary current maxima occurring at potentials for which the non sensitized alloy is passive. A detailed critique of the explanations of this secondary maxima is given elsewhere.[2,3] As shown by Kelly et. al.,[2,3] the most likely explanation of the secondary maxima is that it is a result of the superposition of two anodic currents, one from the bulk alloy and one from a chromium-depleted zone next to the grain boundaries as proposed previously[14], although the Kelly, et. al. results could not directly contradict the explanation that the secondary maxima is induced by the oxidation of ferrous ions in the solution.[15] Kelly et. al.,[2,3] showed that the maximum IGC was observed in Type 430 stainless steel (430 SS) which was held at 550°C for 2 hours as shown by the polarization curves, current vs. time curves, and morphological studies.

EXPERIMENTAL PROCEDURE

Polarization Curves

The Type 430 stainless steel samples of size 2.5 x 1.3 x 1.3 cm^3 and composition given in Table 1 were encapsulated in clear fused quartz tubing under a vacuum of 10^{-2} torr, solution annealed at 1200°C for 1 hour and quenched in ice water. The samples were then similarly encapsulated and sensitized at 550°C for 2 hours and ice water quenched. The samples were then mounted using double sided tape and one side polished to 240 grit and the other polished to 600 grit, degreased with reagent grade acetone and ethanol in an ultrasonic cleaner for 20 minutes. The 1N H_2SO_4 (pH = 0.18) solution was prepared using reagent grade H_2SO_4 and high purity water (18MΩ resistivity). Copper wires were soldered using Sn/Pb solder (Kestor Solder, Des Plaines, IL) or spot welded to the specimen and the connection edges and back masked with lacquer to expose a nominal area of 3.25 cm^3 of the 600 grit polished surface. The solution was deaerated for 2 hours using purified nitrogen prior to the experiment. The sample was held at -1000 mV_{SCE} for 1 minute to remove any oxide film and allowed to equilibrate at open circuit for 10 minutes, and then anodically scanned from the open circuit potential to +1400 mV_{SCE} at a scan rate of 0.1 $mV\ s^{-1}$.

IGC/Permeation Experiment

The permeation setup is shown in Figure 2. For the corrosion cell a model 173 PAR potentiostat was used to maintain the surface of the sensitized sample in the anodically polarized condition at -50 mV_{SCE}/+192 mV_{SHE} while using a Hewlett Packard 3468A current meter to measure the (anodic) current. On the exit surface where the arriving H atoms are to be oxidized, a 173 potentiostat is used to maintain the exit surface at a potential favorable for oxidation of any arriving hydrogen, a 3468 Hewlett Packard current meter is used to measure the permeation current, i_p, and a Fisher 5000 chart recorder with a sensitivity of 0.001 μA is used to record the permeation current, i_p. The exit surface is coated with Pd (electroless Pd, Technic Inc.) to prevent

oxidation of the alloy. Since both potentiostats had a common working electrode, the exit cell potentiostat was floated from ground using an isolation transformer and 12 μF pyranol capacitor.

Pre-electrolysis of the 1N H_2SO_4, pH = 0.18, used in the corrosion cell and of the 0.1 N NaOH, pH = 12.8, used in the H oxidation cell is carried out at a current density of 1 mA cm^{-2} using a Hewlett Packard constant current source 6186C along with constant deaeration by purified nitrogen gas. Pre-electrolysis is carried out for 72 hours. After pre-electrolysis the solutions are directly transferred into their respective compartments under N gas following the procedure outlined below.

First, the exit solution is let into the exit cell, the exit surface being maintained at +200 $mV_{Hg/HgO}$ (potentials ±100 mV of this potential gave the same steady state permeatear current i_∞). The i_p is allowed to decay to below 0.5 μA to establish a background level. Then the charging solution is let into the corrosion cell and the input surface is immediately poised potentiostatically at -50 mV_{SCE}/+192 mV_{SHE}.

RESULTS AND DISCUSSION

The polarization curves for three sensitized samples are shown in Figure 3. As can be seen in Figure 3, the reproducibility is good. Polarization curves for nominally non sensitized Type 430 stainless steel were similarly obtained by carrying out the same experimental procedure on the as received material and are shown in Figure 4. The two curves for the nonsensitized samples generally agree with the standard ASTM curve[16] for Type 430 stainless steel in deaerated 1N H_2SO_4 at 30C using 0.1 mV s^{-1} scan rate, also shown in Figure 4. The difference between the passive currents of samples 1 and 2 may be due to the fact that run 2 was carried out by repolishing sample 1 and not by using a new specimen as was done in obtaining the polarization curves in Figure 3. The minimum at approximately -200 mV, SCE, has been observed before in Fe-Cr alloys.[17] This has been explained by Edeleanu[18] and is the result of the hydrogen evolution reaction (h.e.r.) contribution to the total (ammeter) current at potentials up to its equilibrium potential which is positive of the passivation potential.

Comparing Figures 3 and 4, one can observe that the secondary maxima is much more pronounced for the sensitized steel, and is attributed to anodic dissolution of the Cr-depleted alloy. Passivation of the lower Cr containing region at a more positive electrode potential than for the alloy itself is consistent with the known strong dependency of the passivation potential on the chromium content.[19] The small secondary maxima in the non sensitized steel can be explained by the fact that even during the casting of the steel a finite time is required to quench the samples down to the temperature below which carbide precipitation does not occur so that a slight sensitization occurred.

As can be seen in Figure 3, the secondary maxima occurs at approximately -50 mV_{SCE}/+192 mV_{SHE}. This potential was chosen in the IGC/permeation experiment as the potential for anodic polarization of the sensitized Type 430 stainless steel, as this potential is much more positive than the h.e.r. potential for the 1N H_2SO_4 electrolyte, is in the passive region of the bulk alloy, and is in the active region of the Cr-depleted metal along the grain boundary. It follows that with the outer surface held at -50 mV SCE, IGC occurs initially by anodic dissolution of the Cr-depleted metal and the h.e.r. does not occur. Then, the only way hydrogen permeation can be measured on the exit side is if the IR mechanism of active metal dissolution[4-12] occurs in the grain boundary grooves formed by attack of the chromium depleted zone. At the potentials of base metal dissolution in the active loop, the local electrode potential in the groove is also negative of the hydrogen potential so the h.e.r. also occurs. The latter can only happen if an IR drop in the groove shifts the electrode potential from the positive value above the h.e.r. potential at the surface of the specimen to potentials below the h.e.r. potential inside the groove. This is also the potential region of active dissolution of the alloy (Fig. 3). Such an IR drop phenomena is now known to be the cause of crevice corrosion of iron[4-9], and, similarly, hydrogen gas bubbles were observed to form on the crevice walls during the crevice corrosion process. In several experiments using the arrangement in Fig. 1b, hydrogen permeated through the sample thickness and a current was measured on the exit side. A typical hydrogen permeation result is shown in Figure 5. After approximately two minutes, hydrogen arrives at the other side of the sheet specimen and the

current increases as arriving hydrogen atoms are oxidized by the 200 mV Hg/HgO potential maintained on the (exit) surface. After the initial steep increase, the current continues a more gradual rise for the duration of the experiment.

Detection of a permeation current in the exit oxidation cell proves that the hydrogen evolution reaction (h.e.r.) is occurring within the grain boundary grooves. Although the steel input surface was maintained under anodic polarization at the more positive potential in the passive region, the electrode potential in the crevice formed by the grain boundary grooves was at less noble values, below the h.e.r. potential, resulting in hydrogen evolution and permeation and, as Kelly, et al., concluded[2], anodic dissolution of the sample by the IR mechanism in place of the Cr depletion mechanism. Thus, the bulk grains of normal Cr content are also readily attacked.

In summary, in an anodically polarized specimen, both the h.e.r. and anodic metal dissolution by the IR mechanism start after the grain boundary grooves are formed by anodic dissolution of the Cr-depleted alloy. The IR mechanism readily attacks the stainless steel grains of normal Cr content. In view of the more negative potential in the grooves, dissolution of the Cr-depleted alloy will still occur but not in a selective manner, i.e., the Cr-depletion mechanism ceases to operate in regions where the IR mechanism operates.

CONCLUSIONS

1. Intergranular corrosion of sensitized Type 430 stainless steel involves a second corrosion process, besides the anodic dissolution of the chromium depleted zone.
2. Hydrogen ion reduction was shown to be occurring inside the grain boundary grooves by detecting a hydrogen permeation current using an electrochemical permeation technique.
3. Since proton reduction could only occur if the electrode potential in the grooves was much less noble than the applied value at the outer surface, detection of the hydrogen permeation current is a proof that the second corrosion process is stabilized by the IR mechanism of localized corrosion.

ACKNOWLEDGMENT

Support of the Office of Naval Research, Contract No. N00014-91-J-1189

(A. J. Sedriks) is gratefully acknowledged.

REFERENCES

1. B. W. Bennett and H. W. Pickering, Metallurgical Trans. A, 18A, 1117 (1987).
2. W. K. Kelly, R. N. Iyer and H. W. Pickering, submitted to J. Electrochem. Soc.
3. M. Zamanzadeh, R. N. Iyer, W. K. Kelly and H. W. Pickering, Proc. Intern. Symp. on Testing and Failure Analysis, ISTFA 1988, ASM, Metals Park, OH, 1988, p. 425.
4. A. Valdes-Molden, Ph.D. Thesis, The Pennsylvania State University, 1986.
5. A. Valdes and H. W. Pickering, Advances in Localized Corrosion, H. Isaacs, U. Bertocci, J. Kruger and S. Smialowska, eds. NACE-9, Natural Association of Corrosion Engineers, Houston, TX, 1990, p. 393, ibid, p. 77.
6. H. W. Pickering, Corrosion Sci. 29, 325 (1989).
7. K. Cho and H. W. Pickering, J. Electrochem. Soc., 138, L56 (1991); ibid, 137, 3313 (1990).
8. K. Cho, H. W. Pickering and E. Nystrom, Corrosion Sci., in press.
9. K. Cho and H. W. Pickering, Critical Factors in Localized Corrosion, G. Frankel and R. Newnman, eds., Vol. 92-9, The Electrochemical Society Softbound Proceedings Series, Pennington, NJ, 1992, p. 407.
10. M .Wang, Y. Xu and H. W. Pickering, in preparation.
11. Y. Xu and H. W. Pickering, J. Electrochem. Soc., 140, 658, (1993).
12. Y. Xu and H. W. Pickering, Critical Factors in Localized Corrosion, G. Frankel and R. Newnman, eds., Vol. 92-9, The Electrochemical Society Softbound Proceedings Series, Pennington, NJ, 1992, p. 407.
13. M. A. Devanathan and L. Stachurski, J. Electrochem. Soc., 111, 619 (1964).
14. P. Suery and T. Geiger, Werkstoffe und Korrosion, 20, 665 (1969).
15. O. L. Riggs, Jr., Corrosion, 31, 413 (1975).
16. ASTM G5-87, 1991 Annual Book of ASTM Standards, Vol. 3.02, ASTM, Philadelphia, PA.
17. H. W. Pickering and R. P. Frankenthal, J. Electrochem. Soc., 112 761 (1965).
18. C. Edeleanu, Nature, 173, 739 (1954); Iron and Steel Inst., 188, 122 (1958).
19. R. P. Frankenthal and H. W. Pickering, J. Electrochem. Soc., 120, 23 (1973).

Table 1. Composition of a Type 430 stainless steel provided by the supplier.

Cr	16.46%
C	0.055 wt%
Mn	0.48 wt%
Mo	0.024 wt%
N	0.017 wt%
Ni	0.32 wt%
P	0.035 wt%
S	0.004 wt%
Si	0.36 wt%
Fe	balance

FIGURE CAPTIONS

Figure 1. Schematic diagrams for permeation of hydrogen through a metal membrane. (a) Input surface is cathodically polarized. (b) Input surface is anodically polarized resulting in anodic dissolution of the Cr-depleted alloy to produce the IR condition for the h.e.r. and anodic dissolution of bulk alloy.

Figure 2. Schematic of the hydrogen permeation apparatus.

Figure 3. Anodic polarization curves for three different samples of sensitized (550°C for 2 hours) Type 430 stainless steel in 1 N H_2SO_4.

Figure 4. Anodic polarization curves for two samples of as received (non-sensitized) Type 430 stainless steel in 1 N H_2SO_4 and the standard ASTM plot.[16]

Figure 5. A typical hydrogen permeation result for anodic polarization of a sensitized Type 430 stainless steel in 1 N H_2SO_4 (scheme in Figure 1b).

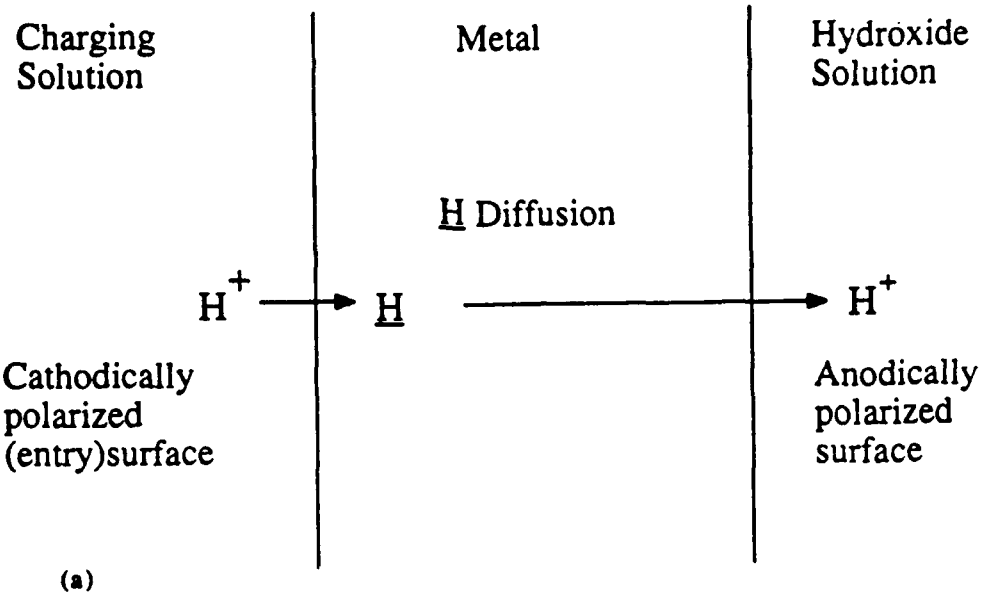

(a)

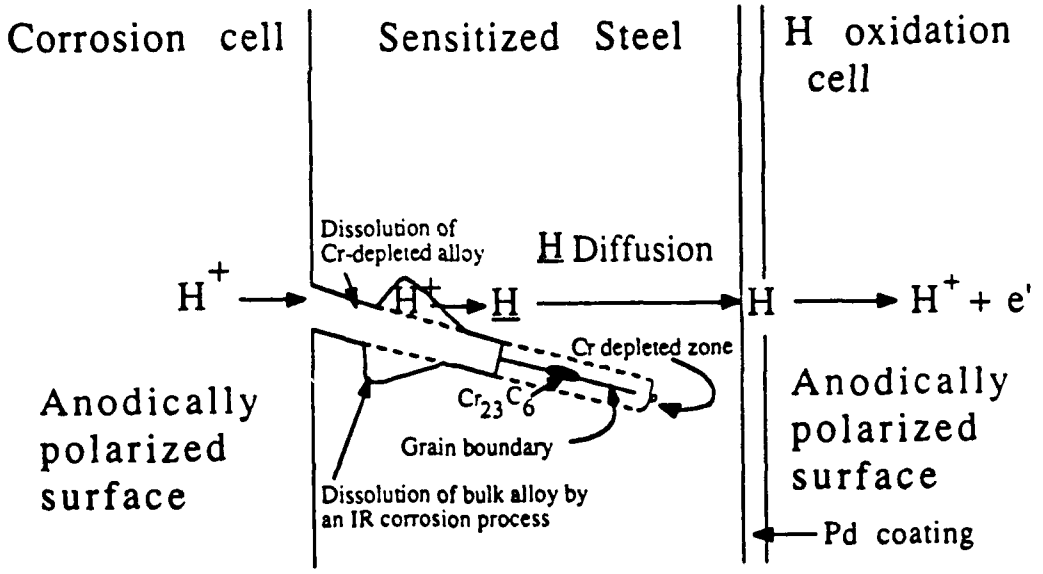

(b)

FIG 1 Sehgal, et. al.

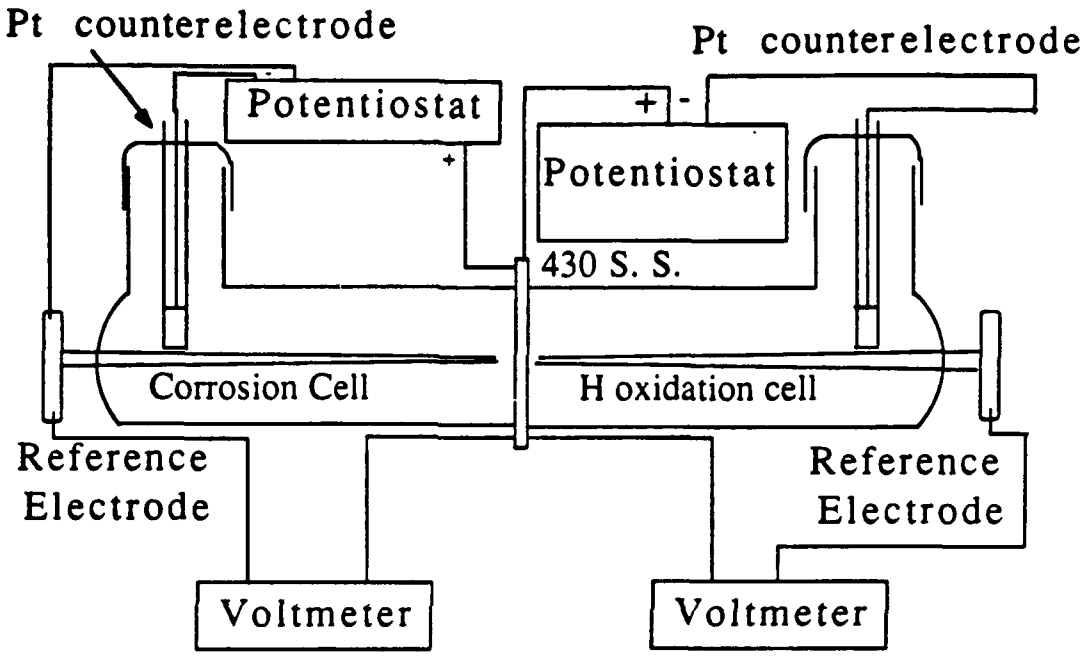

FIG. 2. Sehgal, et. al.

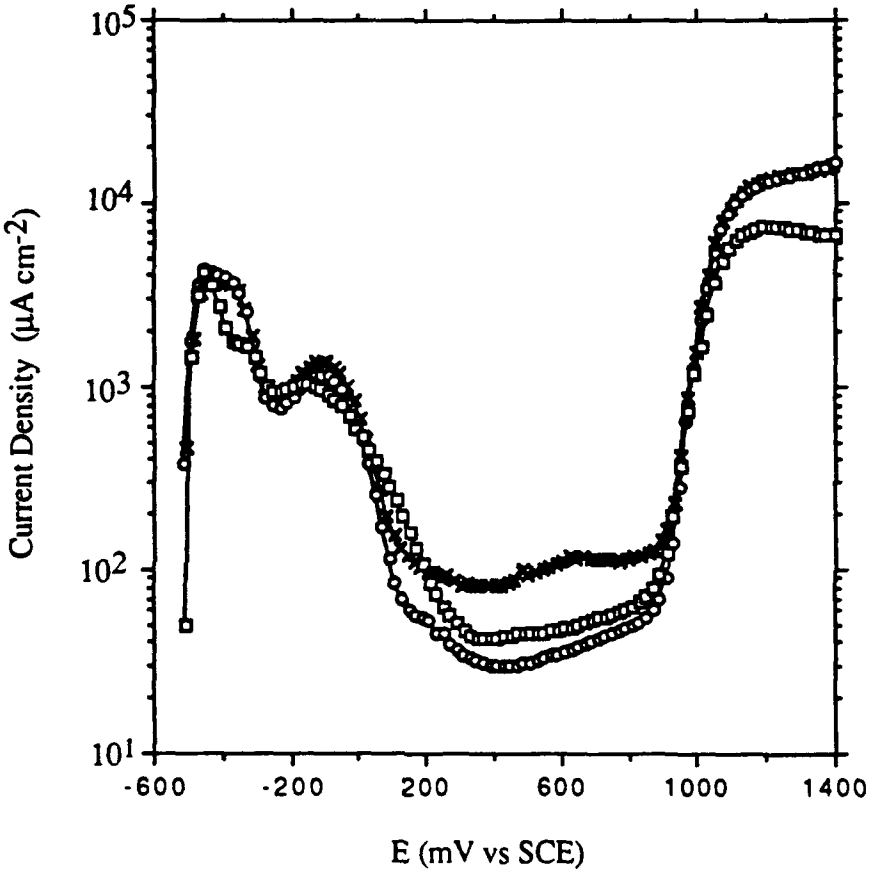

FIG 3 Sehgal, et. al.

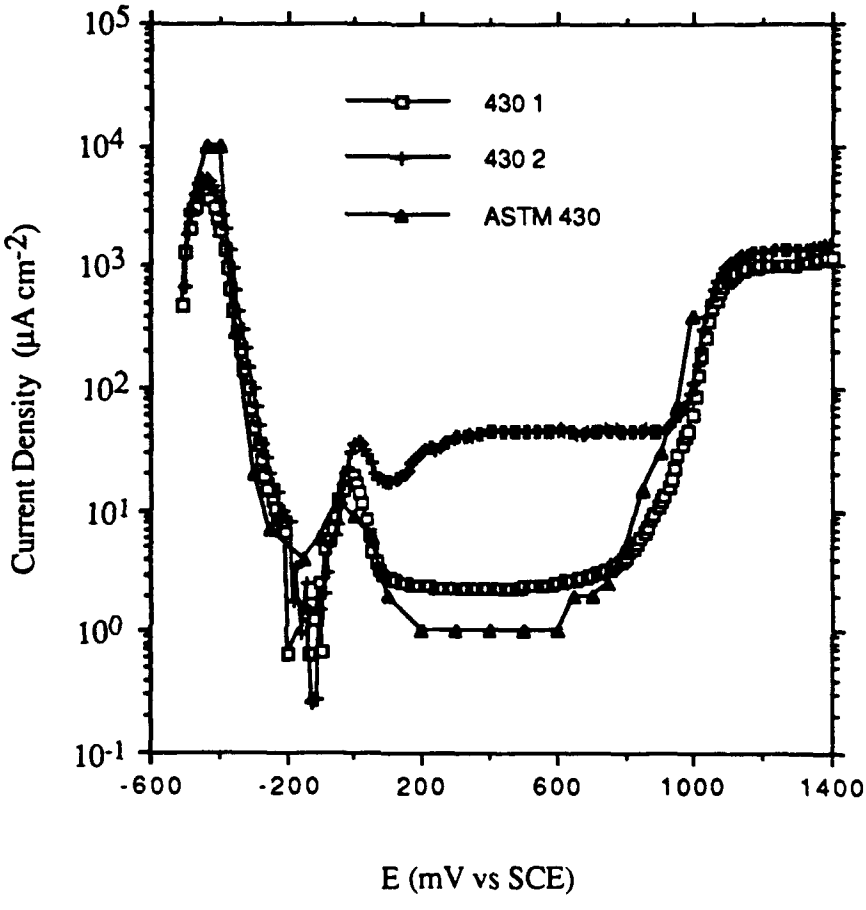

FIG 4, Sehgal, et.al.

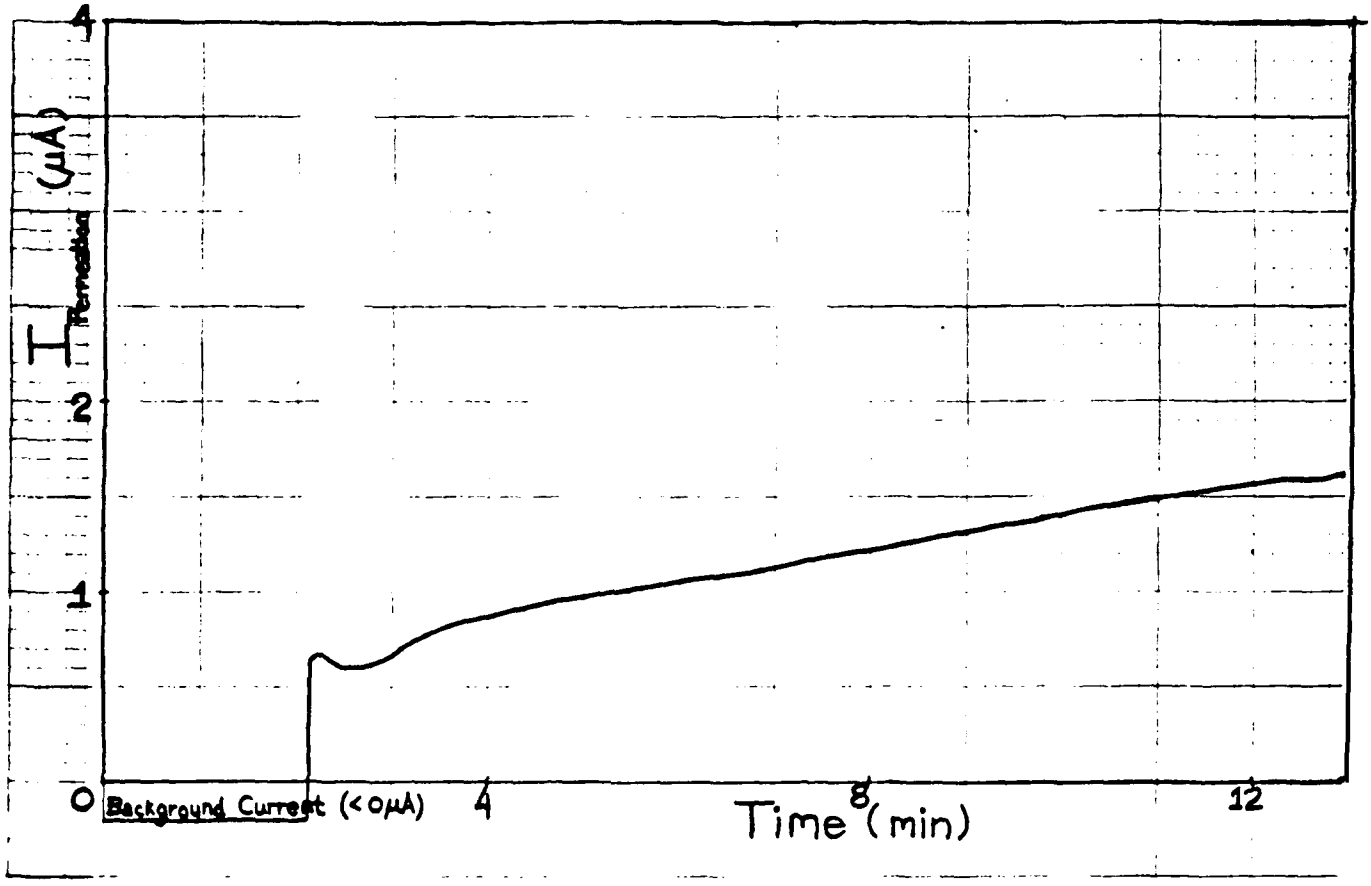

FIG. 5 Sehgal, et.al.

SECTION 3

ANOTHER GRAIN BOUNDARY CORROSION PROCESS IN SENSITIZED STAINLESS STEEL

William K. Kelly, Rajan N. Iyer and Howard W. Pickering
Department of Materials Science and Engineering
The Pennsylvania State University
University Park, PA

ABSTRACT

This work investigates the intergranular corrosion of a sensitized Type 430 stainless steel in 1N H_2SO_4. Once the grain boundary groove is formed by dissolution of the Cr-depleted material, a second form of localized corrosion commences within minutes and replaces the Cr-depletion mechanism. The second mechanism attacks both the bulk grains (of normal Cr content) and the Cr-depleted alloy. This is shown by groove widths that are as much as 40 times the Cr-depleted zone widths. Gas bubbles deduced to be hydrogen, egress from the grain boundary grooves, indicating a sizable potential drop within the grooves and the likelihood that the second corrosion process is caused by the IR phenomenon recently found to account for crevice corrosion in iron. The same mechanism could account for the observed corrosion under the lacquer at the sample edges.

INTRODUCTION

The intergranular corrosion of stainless steels has been explained by the chromium depletion theory first shown by Strauss et al (1) and Bain et al (2) for austenitic stainless steels and proposed by Baumel (3) for ferritic stainless steels. Additional experimental evidence that this theory applies to ferritic stainless steels was given by Bond (4) and more extensively by Frankenthal and Pickering (5). Stated briefly, the chromium depletion theory claims that the formation of chromium carbides at the grain boundaries of a stainless steel will cause the alloy adjacent to the boundaries to be depleted of chromium. The potential region of stability of the passive film is known to be a strong function of the chromium content, decreasing in size with decreasing chromium content (5). Thus, if there is insufficient chromium in the Cr-depleted region, this

region will not form a stable passive film (at the corrosion potential) and will dissolve leaving grooves along the grain boundaries.

Bennett and Pickering (6) noticed in their studies of grain boundary corrosion of sensitized austenitic stainless steels that the resulting grain boundary grooves were wider than the predicted depleted zone width. Thus, bulk alloy with its normal chromium content was seemingly being attacked, a result not explained by the chromium depletion theory. They concluded that a second corrosion process occurred along with dissolution of the chromium depleted alloy to significantly increase the grain boundary attack. More recently, Zamanzadeh et al. (7) observed the same in an investigation of a stainless steel tube which failed in service due to intergranular corrosion (IGC) in acid solution.

Thus, one explanation of the unexpectedly large grain boundary grooves in sensitized alloys is that another form of localized corrosion commences during or after dissolution of the Cr-depleted material. Alternatively, a wider-than-calculated zone of Cr-depletion develops during the sensitization heat treatment, i.e., other factors in additions to the diffusivity of chromium, are involved in the sensitization process, such as the occurrence of diffusion induced grain boundary motion (DIGM). The goals of this study were to (i) confirm the Bennett and Pickering observations and (ii) identify the cause of the larger-than-expected grain boundary grooves.

EXPERIMENTAL PROCEDURE

Samples of a Type 430 stainless steel with a composition given in Table 1 were cold rolled (60% reduction) to 0.5 mm thickness, cut to roughly 1 cm by 1 cm, vacuum encapsulated after purging with helium, solution annealed at 1200°C for 1 hour and water quenched, and finally sensitized at 550°C for 1 or 2 hours. A few samples were partially or fully healed by holding for longer times at 550°C. After removal from the capsules and mechanical polishing, the samples were anodically polarized in either a standard 3-electrode corrosion cell deaerated with argon or in an open petri dish in 1N H_2SO_4 solution (in some experiments NaCl was added), and the current was measured as a function of time. For the polarization curves a scan rate of 0.1 mV s^{-1} was

used after immersing the sample in the cell for approximately 10 minutes at open circuit followed by 10 minutes at -600 mV SCE. Electrical connection to the samples was made by spot welding a copper wire to the corner of the sample and masking the wire and the back and sides of the sample with lacquer. This left about 0.8 cm^2 of sample surface exposed to solution. The petri dish set-up included a microscope for direct in-situ viewing of the sample surface, as shown in Figure 1. The potential used was -100mV SCE for most experiments. According to Figure 2 this potential should cause rapid dissolution of Fe-Cr alloy containing less than about 12wt% Cr whereas alloy containing more than 12wt% Cr should passivate (5). The polarization curves reported below also indicate that for -100 mV SCE, the sensitized metal along the grain boundaries should actively dissolve while the bulk grains containing the normal Cr content should be in the passive state.

RESULTS

Figure 3 shows the polarization curves of Type 430 stainless steel in 1N H_2SO_4 with different degrees of Cr-depletion at the grain boundaries, ranging from severe for the sensitized condition to little if any for the healed condition. The anodic peak centered at -100 mV SCE for the sensitized heat treatment condition is absent for the healed condition, consistant with the interpretation that this peak is produced by anodic dissolution of the Cr-depleted material along the grain boundaries (8,9).

During anodic polarization of the sensitized samples at -100 mV SCE, insitu microscopic examination using the arrangement shown in Figure 1 reveals attack of the grain boundaries but not of the grain surfaces, and also the eventual egress of gas bubbles from within the grooves. The current during the experiment is initially roughly constant for 1-5 minutes and then abruptly begins to increase. A typical current-time behavior for the sensitized samples is shown in Figure 4. For the solution annealed condition, the anodic dissolution current at -100 mV SCE is more than an order-of-magnitude lower than for the sensitized condition (Figure 4), and is another order-of-magnitude lower for the healed condition. For both the solution annealed and healed conditions no rise in current occurs at later times in the experiments.

Figure 5 shows cross sectional views of grain boundaries after intergranular corrosion during anodic polarization at -100mV SCE. According to a kinetic model of Iyer and Pickering (10) which has been verified by comparison with the experimental data of Hall and Briant (11), the depleted zone width on each side of the grain boundary should be approximately 600Å and the carbide thickness approximately 400 Å. Even though the carbides remain undissolved, they will form a part of the observable grooves, either because they are dislodged during the corrosion process or are not resolved during microscopic examination. Thus, the expected groove width for corrosion of all of the Cr-depleted metal is approximately 1600Å. Figure 5a shows that the groove width in some subsurface regions after 30 minutes is as large as 12,000Å which is over 7 times the depleted zone width. With increasing time the subsurface regions of attack grow larger whereas no further widening of the grooves occurs near the outer surface, Figures 5b-d. The largest measured groove widths were 53,000Å and 80,000Å which are 33 and 50 times the depleted zone width, respectively. These results were the same whether obtained in the deaerated cell or in the air exposed petri dish. Clearly these results strongly suggest that most of the dissolution producing the gross subsurface cavities is of bulk alloy rather than Cr-depleted alloy, since the width of the Cr-depleted zone can hardly be so large or so uneven.

Additional longer term experiments were carried out to see if dissolution of the bulk alloy continued. In an experiment in which a sample was held at -100mV SCE in 1N H_2SO_4 + 0.05N NaCl for 143 hours until nearly complete disintegration, 262 coulombs of charge were passed. This is 20 times that expected if only the Cr-depleted zone dissolves.* This experiment was repeated for a sample held in 1N H_2SO_4 at -100mV SCE for 6 hours and then at 200mV SCE for several days until nearly complete disintegration; the total charge passed was 191 coulombs, which is approximately 15 times that expected if only Cr-depleted alloy dissolved. These samples showed almost no change in surface appearance but completely disintegrated at the slightest touch or on removal from the cell.

---

* Assuming that the only anodic reaction is $Fe \Rightarrow Fe^{2+} + 2e^-$, and using the calculated Cr-depleted volume (average grain diameter is 30μm), the Faraday constant, and the molar volume of iron, the charge required to dissolve the entire Cr-depleted zone is calculated as approximately 13 coulombs.

In another experiment a sensitized sample was held at -100 mV SCE to dissolve the sensitized material (and form the grain boundary grooves). Then, the sample was removed from the cell, thoroughly rinsed in distilled water, dried at 150°C for 2 hr to terminate all electrochemical processes, and reimmersed at 200mV SCE. At 200mV SCE, dissolution of Cr-depleted alloy is at best difficult because very little if any of the grain boundary region has such a low Cr content to be active (especially after dissolution at -100 mV SCE) rather than passive at this potential, in accord with Figures 2 and 3. This was confirmed by immersion of fresh (not previously polarized) sensitized samples at 200mV SCE; these samples registered negligible current and in post microscopic examination showed little or no grain boundary attack. On the other hand, when the samples with grooves formed at -100 mV SCE were reimmersed at 200 mV SCE, there occurred a gradual increase in current with time and the eventual evolution of gas bubbles from the grain boundary grooves. When NaCl was added to produce a 0.3N NaCl solution the rise in current with time upon reimmersion at 200mV SCE (442 mV SHE) was much more rapid and the evolution of hydrogen gas bubbles occurred sooner and profusely.

In the experiments, corrosion was observed to occur under the lacquer used to mask the edges of the specimen. Regions under the lacquer near, but not right at, the lacquer edge were more heavily corroded than elsewhere and both the bulk grains and the Cr-depleted alloy were dissolved. An example is shown in Figure 6. The width of the zone (along the lacquer edge) undergoing crevicing was 200 to 300 μm and was located approximately 50 μm from the lacquer edge. In this same area gas bubbles were seen to grow and coalesce into elongated bubbles during the experiments. Since photographs could not be taken during the observations, the gas bubbles do not appear in later photographs but their shape and location has been schematically added to Figure 6.

DISCUSSION

Width of the Cr-depleted Zone

All the samples consistently showed that the vast majority of the attack is underneath the surface of the metal (as shown in Figure 5). This is further evidenced by the fact that given enough time the inside of the sample will be almost completely converted to the oxidized soluble state even though little attack appears on the surface. If DIGM or some other process were responsible for a wider-than-calculated depleted zone width, the attack would not be mainly concentrated underneath the surface of the metal, i.e., the groove would be very wide everywhere including at the surface. For instance in Figure 5a, the groove width at the surface is approximately 2,000Å, about the same width as the calculated depleted zone width, but at a depth of 14 μm the groove width opens up dramatically to 12,000Å. In Figures 5b and 5c the widest part of the grooves are located at depths of 13 μm and 16 μm, respectively. In summary, the location and large size of the cavities, coupled with the much smaller groove widths at the surface, strongly suggests that a much wider-than-calculated depleted zone width, e.g., due to DIGM, is not present in these specimens.

Evidence for a Second Corrosion Process

The above discussion of the width of the Cr-depleted zone shows that the gross subsurface cavities shown in Figure 5 can not be explained in terms of the selective attack of Cr-depleted alloy. Furthermore, there is a second major discrepany between the Cr-depletion mechanism and one of the experimental observations. Gas bubble evolution from within grain boundary grooves is inconsistent with the Cr-depletion mechanism since neither the hydrogen evolution reaction (h.e.r.) nor oxygen evolution reaction is thermodynamically possible at potentials for which the Cr-depleted alloy selectively dissolves (approximately -200 to 50 mV SCE as shown in Figure 3). Gas bubble formation is also inconsistent with the potentials applied at the outer surface in these experiments (-100 or 200 mV SCE). The two current-time behaviors observed for the sensitized condition in Figure 4 is yet a third reason to conclude that a second corrosion process is operating to produce the results in Figure 5.

What is the nature of this other corrosion process and what are the conditions for its occurrence? The observations are: the extra corrosion is completely subsurface, i.e., it is not seen at the surface of the sample although it is conceivable that it may eventually penetrate the surface from underneath, similar to that observed in crevice corrosion (13). The extent of the corrosion attack, however, is unlike classical pitting or crevice corrosion, processes that are not usually associated with the words 'total disintegration' of the sample. Dealloying comes to mind as the one corrosion process that can produce a condition such that the sample outwardly looks in tact but crumbles at the slightest touch. Dealloying, requires that the major alloying components be of widely different electronegativity, preferably with the most electronegative component in the majority (12). Although iron and chromium do differ significantly in electronegativity, iron is the more noble of the two and few if any cases of dealloying have been reported with the more noble component being 82% of the alloy composition (Table 1). Furthermore, the porosity that develops in dealloying is very fine and uniform in size, quite unlike the large, irregular, subsurface cavities seen in Figure 5.

The current-time behavior shows when the second corrosion process commences. For the sensitized condition, a current increase was recorded after a few minutes of roughly constant current. Since attack of the Cr-depleted alloy starts immediately (1-5), the initial constant current is concluded to be the anodic dissolution of the Cr-depleted material at the grain boundaries. The abrupt increase in current then could be the start of the second corrosion process. This deduction is also in accord with the absence of both a current increase and subsurface attack for the other heat treatments (solution annealed and healed). Since these other heat treatments do not cause significant grain boundary corrosion and the formation of deep grain boundary grooves, it follows that the grooves may be a prerequisite for the second corrosion process. Hence, the second corrosion process may be more like crevice corrosion than pitting corrosion, where the grooves at some stage of their formation (by the Cr-depletion corrosion process) achieve the required gap opening and depth (aspect ratio) to support an active crevice-type corrosion process (13-19).

As a result of the high density of grain boundary intersections with the surface, grain boundary grooves form and, consequently, numerous IR-induced corrosion penetrations occur into the bulk grains of normal Cr content. This high density of crevice-like corrosion processes could produce the total disintegration reported above in the longer term, several day experiments.

The IR Mechanism of Corrosion

If the second process is a clone of crevice corrosion, one needs to show the existence of a significant potential drop between the electrolyte at the subsurface anodic sites and the bulk solution. There is now ample evidence that the underlying requirement for crevice corrosion to occur is that the IR voltage drop in the crevice electrolyte places the electrode potential at the anodic sites (within the crevice) at values in the active loop of the crevice electrolyte polarization curve (13-16).

As mentioned above, the observation of gas evolution, either hydrogen or oxygen, during the experiment is inconsistent with the dissolution of Cr-depleted alloy. However, one can rationalize the formation of hydrogen gas by taking into account an IR voltage within the electrolyte inside the groove(13-18). Considering the available reactants (1N H_2SO_4 with and without NaCl) and potential theory which establishes that the electrode potential within recesses is less oxidizing than the applied potential at the outer surface by the amount of the IR voltage within the recess, the formation of hydrogen gas becomes a possibility inside the groove, consistent with its observed location during the experiments. The occurrence of the h.e.r. requires that the electrode potential is more negative than the reversible potential for the h.e.r. (~ - 240 mV SCE for 1N H_2SO_4). Thus, a significant IR voltage must have existed between the outer sample surface (-100 or 200 mV SCE) and the inside of the grooves from which gas bubbles were observed to egress. Gas bubble evolution solely from within the grain boundary grooves was consistently observed for solutions of 1N H_2SO_4 with and without the addition of 0.3N NaCl. Furthermore, the deduction that the gas is hydrogen means the Cr depletion mechanism, per se, ceases to operate at these locations of the h.e.r. inside the grain boundary grooves. The reason is that at potentials of the h.e.r., bulk

alloy of normal Cr content dissolves along with the Cr-depleted alloy (Figure 3), i.e., Cr-depleted alloy is attacked but not selectively at potentials of the h.e.r.

Thus, one may argue that the subsurface nature of the attack progressing from the narrow grain boundary grooves into the bulk grains is caused by a shift in electrode potential into the active loop of the groove electrolyte polarization curve, consistent with the new IR phenomenon of localized corrosion recently proved to be the basis of crevice corrosion in iron (13-16) and previously observed for pit growth in iron (18). What is needed to prove that the electrode potential shifts significantly in the negative (less noble) direction as a function of distance into the grooves is to identify the gas as hydrogen. Gas is also observed regularly in crevice corrosion experiments where the necessary potential shift is directly measurable (13-15). Thus, the formation and growth of gas bubbles within the grain boundary grooves rather strongly implies that a significant potential drop occurs between the outside and inside of the grain boundary grooves. If the gas is hydrogen its evolution at the two quite different applied electrode potentials in these experiments (-100 and 200 mV, SCE), both of which are very positive of the h.e.r. equilibrium potential, shows that large IR drops can occur in the grain boundary grooves for a range of oxidizing conditions at the outer surface.

Although, in general a potential shift which favors cation motion out of a cavity does not rule out an accompanying decrease in pH, acidification of the electrolyte within the groove is hardly a factor in the present experiments, in view of the already low pH of 1N H_2SO_4 which is unfavorable for occurrence of the hydrolysis reaction. Thus, acidification is not required for the electrode potential along the groove wall to shift negatively into the active loop of the polarization curve. The IR phenomenon without accompanying acidification has been experimentally demonstrated during crevice corrosion of iron under conditions for which a decreased pH did not occur in the crevice (13,15). In fact, without hydrolysis just the opposite is expected for iron in 1N H_2SO_4: the calculated ionic concentrations within crevices or pits show that hydrogen ions will tend to migrate out of a cavity under the prevailing potential gradient during anodic polarization (18). This process would raise the pH in the crevice (as would the occurrence of the hydrogen

evolution reaction itself). This rise in pH would occur until the equilibrium pH of the hydrolysis reaction is reached. The pH would then be maintained at this value by the hydrolysis reaction. Thus, no acidification is expected within the grain boundary grooves in this work; rather the pH may rise (~2pH units) to the equilibrium hydrolysis value as shown in what follows.

The possible hydrolysis reactions in the present work are:

$$Fe^{+2} + H_2O \Leftrightarrow FeOH^{+} + H^{+} \qquad K \approx 1.68 \times 10^{-7} \qquad (1)$$

$$Cr^{+3} + H_2O \Leftrightarrow CrOH^{+2} + H^{+} \qquad K \approx 1.54 \times 10^{-4} \qquad (2)$$

For the known equilibrium constants, K, the equilibrium pH can be calculated by assuming unit activity/concentration of the water molecule. If the equilibrium Fe^{+2} ion concentration is y mol/liter, the $FeOH^{+}$ ion will have a concentration of 1-y mol/liter in Reaction (1), and since the H^{+} ion is produced in the same amount as the $FeOH^{+}$ ion, it must also have a concentration of 1-y mol/liter. The H_2O is a pure liquid phase assumed to have an activity equal to 1. Hence, $K = [FeOH^{+}][H^{+}]/[Fe^{+2}] = [1-y][1-y]/y = 1.68 \times 10^{-7}$. Solving for y gives a hydrogen ion concentration of 4.1×10^{-4} mol/liter corresponding to pH 3.4. The same calculation for chromium hydrolysis according to Reaction (2) gives an equilibrium pH 1.9. Therefore, hydrogen ion migration under the potential gradient in the grain boundary groove should raise the pH toward 1.9 or 3.4 depending on the concentrations of the respective metal ions. If the Cr^{+3} concentration in the grain boundary groove is at the equilibrium value for the chromium hydrolysis reaction, then that reaction will control the pH at 1.9. If the Cr^{+3} concentration is not high enough, then the pH will rise to the equilibrium pH for the iron hydrolysis reaction.

Inserting these pH values into the Nernst equation for the h.e.r. gives for the equilibrium potential, E, = -242, -354, and -443mV SCE for pH = 0, 1.9 and 3.4, respectively. These numbers mean that for a grain boundary groove whose pH is controlled between 0 and 1.9 by hydrogen ion migration and consumption on the one hand and the chromium hydrolysis reaction on the other hand, the equilibrium potential for the h.e.r. is between -242 and -354 mV probably being closer to -354 mV SCE. Similarly, for a pH between 0 and 3.4 where the latter is given by the iron

hydrolysis reaction, E is between -242 and -443 mV SCE. These results are shown as cross hatched regions in Figure 7 which is the measured polarization curve for the sensitized sample. Since the equilibrium potentials of the h.e.r. are seen to be in the active loop of the alloy polarization curve, the electrode potential in the grain boundary groove is concluded to be in the region of active metal dissolution. For the non-sensitized material (healed curve in Figure 3) there is no current peak at -100 mV, thereby identifying the current peak at -100 mV as the result of anodic dissolution of the Cr-depleted material; that active dissolution of Cr-depleted alloy occurs in this potential region is also shown in Figure 7 by the accompanying match-up wt% Cr vs. E plot, e.g., at -100 mV, alloy with a Cr content of 11 wt% or less will be in the active dissolution state (5).

The role of chloride in producing more rapid onset and higher rates of corrosion proceeding from the groove into non Cr-depleted alloy (reported above in the experiment in which the sample was reimmersed at 200 mV SCE following a -100 mV treatment that produced the grain boundary grooves) is likely the same as recently discovered during IR-induced crevice corrosion of iron in chloride solution (15). This role of Cl^- involves enlargement of the active loop and an increase in the passive current with increasing Cl^- content. Both facilitate the onset of IR-induced corrosion and higher currents in the active loop enable higher rates of stable (on-going) metal dissolution along the groove wall(15).

In summary, the occurrence of the IR mechanism of localized corrosion requires first a recess in the surface. Intergranular corrosion produces a groove at the grain boundary that could provide for the IR condition as defined elsewhere (14). Thus, sensitized stainless steel may eventually meet this condition when exposed to a corrosive solution. In this paper corrosion of the Cr-depleted zone produced a narrow groove which then served as the vehicle for onset of the IR mechanism of corrosion. This conclusion is based in large part on a theoretical analysis, rather than an experimental proof, that the gas observed evolving from the grooves was hydrogen. Acidification was not a factor in initiating or maintaining this stable IR form of grain boundary corrosion of both bulk alloy and Cr-depleted alloy, since neither the Cr nor Fe hydrolysis reactions can occur at the low pH of the bulk solution. This same corrosion process involving a potential-

shift phenomenon but without acidification of the groove electrolyte (and without aggressive ion build up in the groove) has been discovered and proven to operate during crevice corrosion of iron in both acid and alkaline solutions (13,15).

Both the heavily attacked zone and the formation of gas under the lacquer (Figure 6) are also consistent with the IR mechanism of localized corrosion. This process involves the penetration of electrolyte into the interface area between the lacquer and the sample surface, the establishment of a potential drop placing the local electrode potential under the lacquer in the active region of the cavity electrolyte polarization curve, and a resultant high metal dissolution rate characteristic of the active loop. The existence of the potential drop was shown by the evolution of gas, deduced to be hydrogen for the reasons given above. The edge of the dissolved region under the lacquer also runs parallel to the edge of the lacquer and is highly reminiscent of the well defined distance into a crevice below which crevice corrosion occurs by the IR drop mechanism (15,16).

CONCLUSIONS

The conclusions of this study of intergranular corrosion of a sensitized ferritic stainless steel are:

1. The grain boundary grooves are too large, too uneven in width, and the total charge passed too great to be attributed solely to dissolution of chromium-depleted alloy.
2. A second localized corrosion process commences within the groove after it is formed by the classical Cr-depletion grain boundary corrosion process, and the latter ceases to operate. This subsequent corrosion process accounts for the greater-than-expected groove widths since it readily attacks both the bulk grains of normal Cr content and the Cr-depleted alloy. An IR-induced form of localized corrosion (recently proven to account for crevice corrosion in iron) that commences once the grain boundary groove of certain gap-to-depth dimensions is formed (13-16) is consistent with the data. The existence and identity of this second form of grain boundary corrosion is based on the following experimental observations:

i). the large, uneven and occluded nature of the grain boundary grooves involving alloy that is not depleted in Cr,

ii). two distinct regions in the current-time behavior of the grain boundary corrosion process,

iii). the evolution of gas bubbles from within the grooves; if the gas is hydrogen as expected, the electrode potential within the groove is significantly more negative than the applied potential at the outer surface and,

iv). the occurrence of grain boundary attack at 200 mV (SCE), a potential for which grain boundary corrosion due to Cr-depletion does not occur.

3. Corrosion is also observed at the sample edges under the lacquer. The observation of gas bubble formation under the lacquer and the location of the corrosion with respect to the lacquer edge again indicates the IR mechanism of localized corrosion.

4. Acidification does not occur in the grain boundary grooves (or under the lacquer) since the bulk solution pH is too low for hydrolysis to occur. Thus, the IR-induced potential-shift mechanism without contributions from acidification (or aggressive ion buildup in the absence of aggressive ions in the bulk solution) satisfactorily accounts for the stability of the second grain boundary corrosion process.

5. DIGM cannot explain any of the above observations, although it is not ruled out as a cause of somewhat increased widths of Cr-depleted zones.

ACKNOWLEDGMENT

James Shafer and Akshey Sehgal helped with technical and editorial aspects of the project, respectively. Support of the Office of Naval Research, Contract No. N00014-84-k-0201, is gratefully acknowledged.

REFERENCES

1. B. Strauss, H. Schottky, and J. Hinnuber, Z. anorg allgem. Chem., **188**, 309 (1930).

2. E. C. Bain, R. H. Aborn, and J. J. B. Rutherford, Trans. Am. Soc. Steel Treating, **21**, 481 (1933).

3. A. Baumel, Arch. Eisenhuttenw., **34**, 135 (1963).

4. A. P. Bond, Trans. Metallurgical Soc. AIME, **245**, 2127 (1969).

5. R. P. Frankenthal and H. W. Pickering, J. Electrochem. Soc., **120**, 23, (1973).

6. B. W. Bennett and H. W. Pickering, Metallurgical Trans A, **18A**, 1117 (1987).

7. M. Zamanzadeh, R. N. Iyer, W. K. Kelly and H. W. Pickering, Proc. Intern. Symp. on Testing and Failure Analysis, ISTFA 1988, ASM, Metals Park, OH, 1988, p. 425.

8. P. Suery and T. Geiger, Werkstoffe and Korrosion, **30**, 665 (1969).

9. M. B. Rockel, Corrosion, **27**, 95 (1971).

10. R. N. Iyer and H. W. Pickering, to be published.

11. E. C. Hall and C. L. Briant, Metallurgical Trans A, **15A**, 1703 (1985).

12. H. W. Pickering, Corrosion Sci. **23**, 1107 (1983).

13. A. Valdes and H. W. Pickering, Advances in Localized Corrosion, NACE-9, H. Isaacs, U. Bertocci, J. Kruger, and S. Smialourska, eds., National Association of Corrosion Engineers, Houston, Texas, p. 393 (1990); H. W. Pickering, ibid, p. 77.

14. H. W. Pickering, Corrosion Science, **29**, 325 (1989).

15. K. Cho and H. W. Pickering, J. Electrochem. Soc., **138**, L56 (1991); ibid, **137**, 3313 (1990).

16. Y. Xu and H. W. Pickering, J. Electrochem. Soc., **140**, 658 (1993); ibid, Critical Factors in Localized Corrosion, G. Frankel and R. Newman, eds., Vol. 92-9, The Electrochemical Society Softbound Proceedings Series, Pennington, NJ, 1992, p. 407.

17. J., C. Walton, Corrosion Sci., **30**, 915 (1990).

18. H. W. Pickering and R. P. Frankenthal. J. Electrochem. Society, **119**, 1297 (1972).

19. B. G. Ateya and H. W. Pickering, J. Electrochem. Soc., **122**, 1018 (1975).

Table 1. Composition of Type 430 Stainless Steel Provided by the Supplier

Cr	16.46 wt%
C	0.055 wt%
Mn	0.48 wt%
Mo	0.024 wt%
N	0.017 wt%
Ni	0.32 wt%
P	0.035 wt%
S	0.004 wt%
Si	0.36 wt%
Fe	balance

LIST OF FIGURES

Figure 1 Petri dish experiment for in-situ observation of intergranular corrosion.

Figure 2 Passivation potential vs. wt% Cr for binary Fe-Cr alloys, after Frankenthal and Pickering (5).

Figure 3 Potentiodynamic polarization curves of the Type 430 stainless steel after different final heat treatments in deareated 1N H_2SO_4. (◊) 1200°C for 1 hr and quenched (solution annealed), (♦) 550°C for 2hr (sensitized), (◙) 550°C for 5 hr (partially healed), (■) 635°C for 5 hr, 550°C for 350 hr (healed).

Figure 4 Current density versus time behavior for Type 430 stainless steel at -100 mV SCE in deaerated 1N H_2SO_4 for different final heat treatments: 550°C for 2 hr (sensitized), and 1200°C for 1 hr and water quenched (solution annealed).

Figure 5 Metallographic cross sections after IGC of sensitized (550°C for 2 hr) Type 430 stainless steel showing grain boundary grooves and subsurface regions of gross attack into the bulk grains produced by anodic polarization at -100 mV SCE in 1N H_2SO_4, and a schematic drawing showing the relationship of the observed groove width and the depleted zone width.

Figure 6 Micrograph showing attack of the region under the lacquer near but not directly at the lacquer edge during anodic polarization for 1 hour at -100 mV SCE in 1N H_2SO_4. The location of the gas bubble observed in-situ during the experiments has been schematically indicated on the micrograph.

Figure 7 The relation of the IR drops to the polarization curve for the sensitized condition, and to the wt% Cr in the alloy.

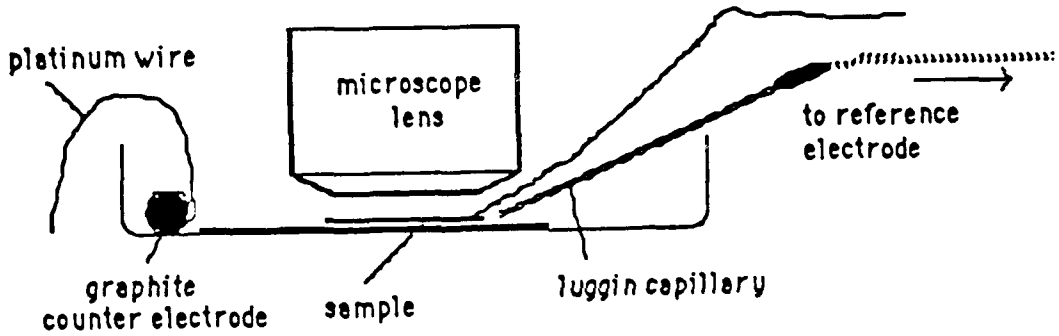

Fig. 1 Kelly, et. al

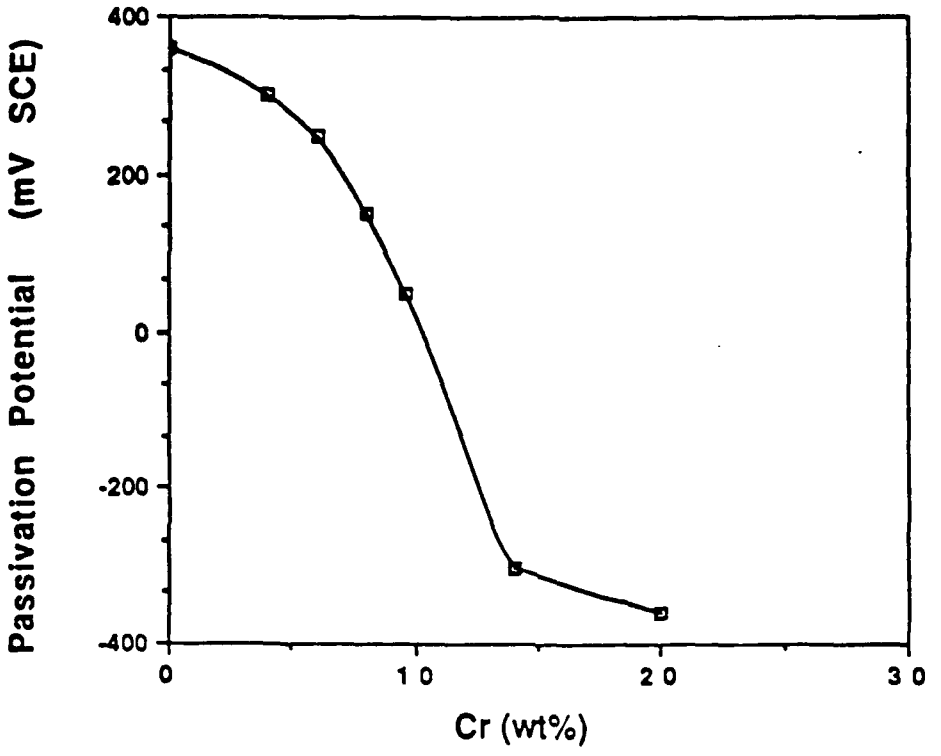

Fig. 2 Kelly et. al.

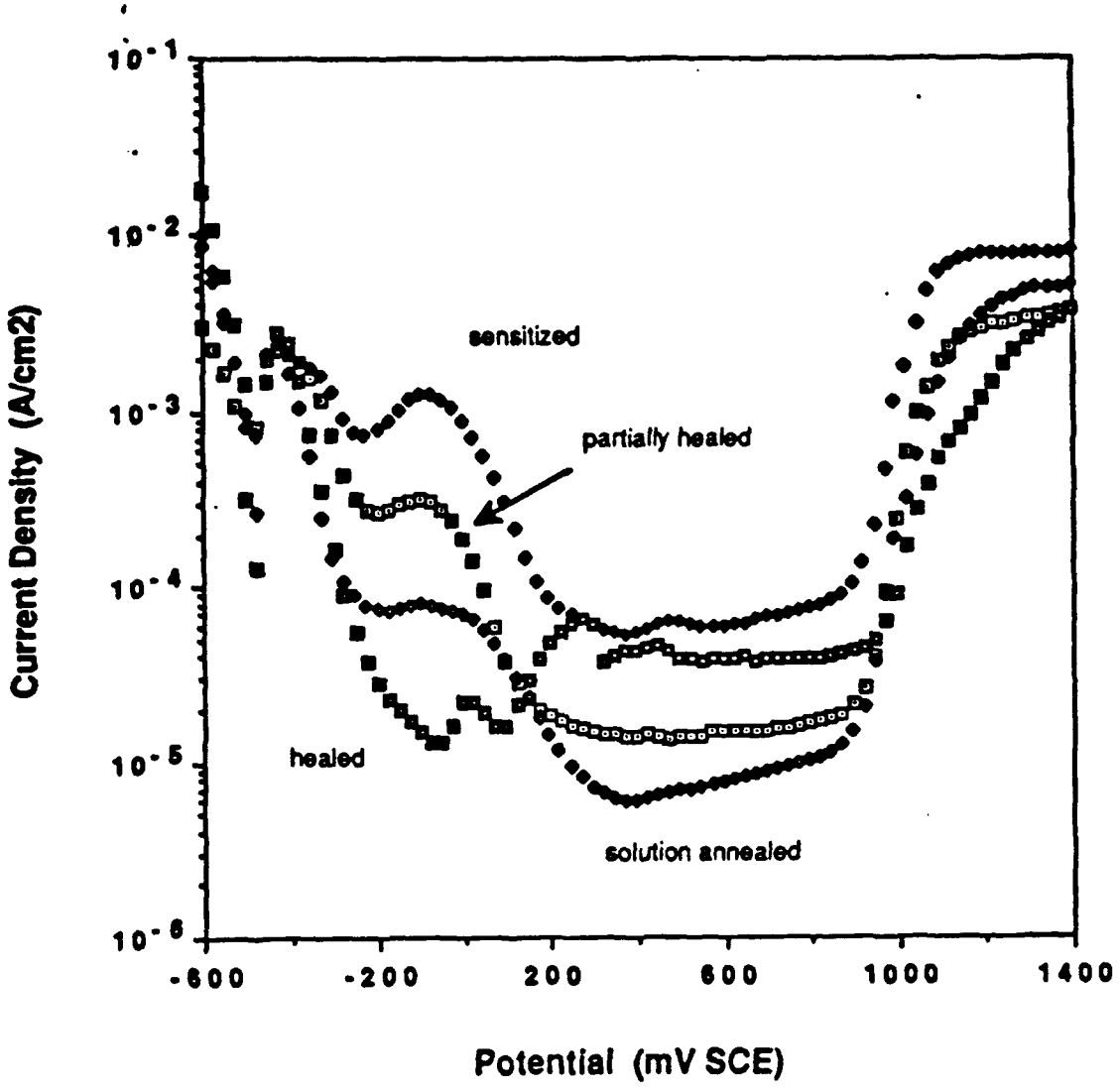

Fig. 3 Kelly, et. al.

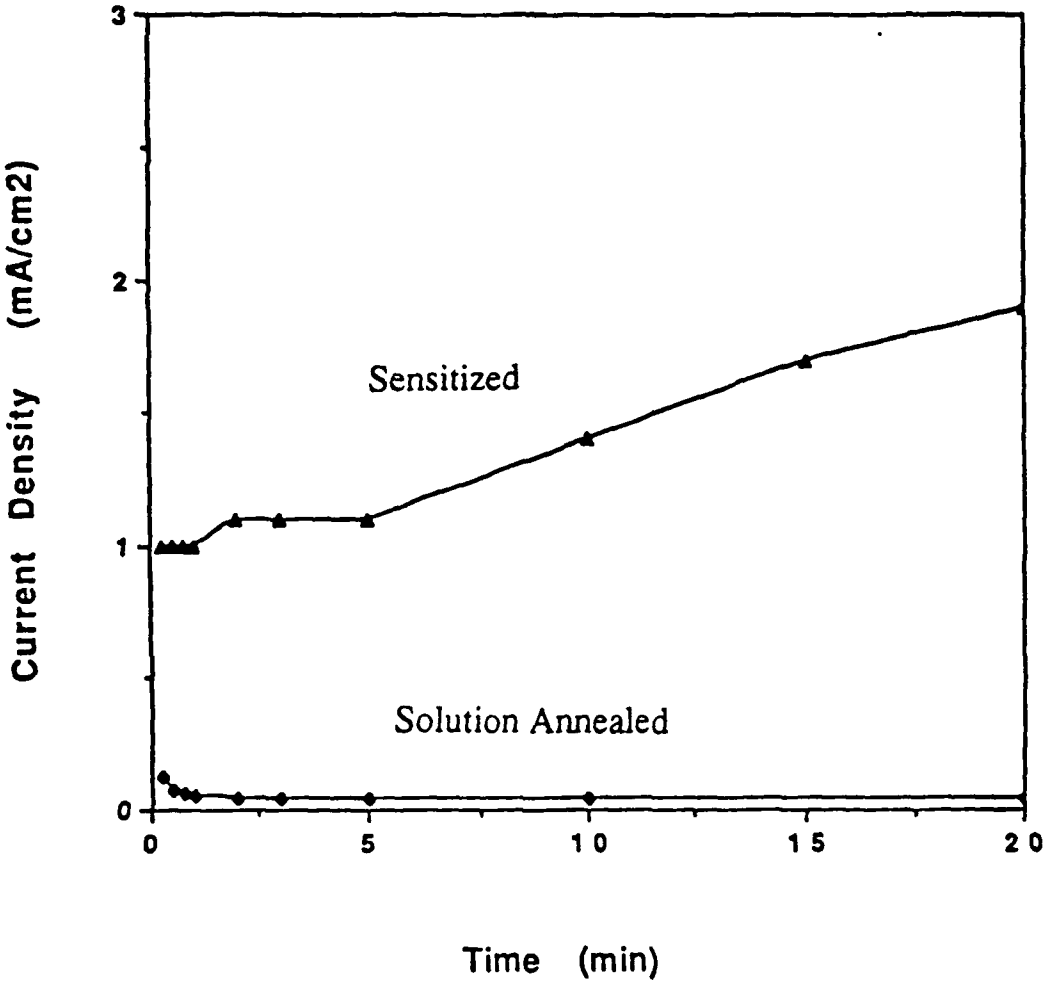

Fig. 4 Kelly, et.al.

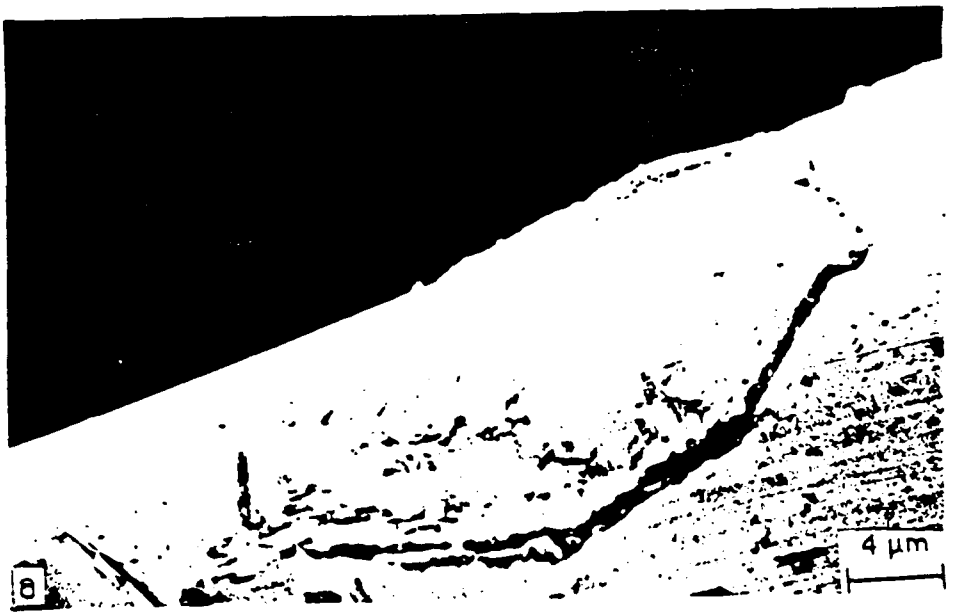
a
4 μm


b
6.7 μm

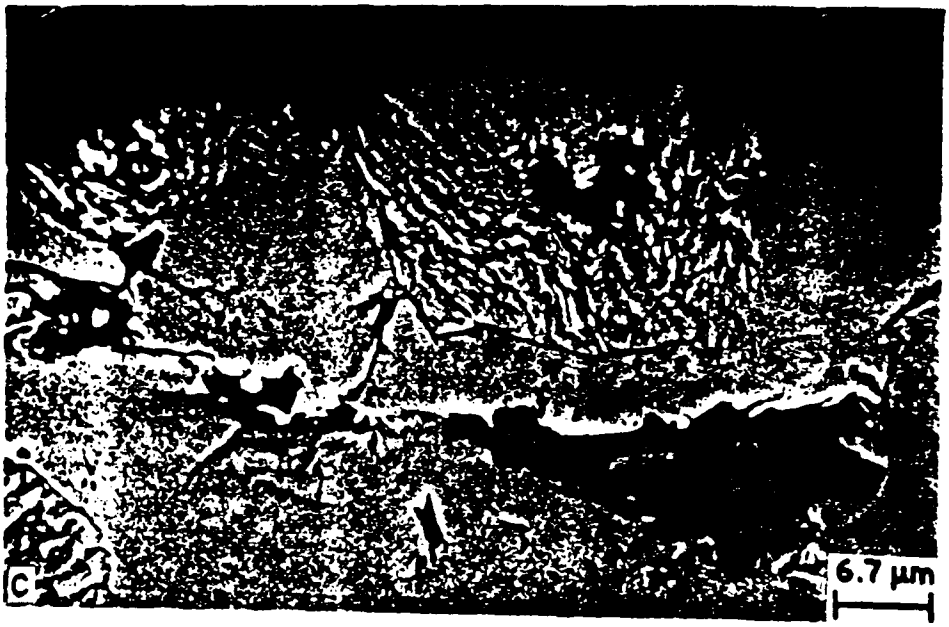
c
6.7 µm

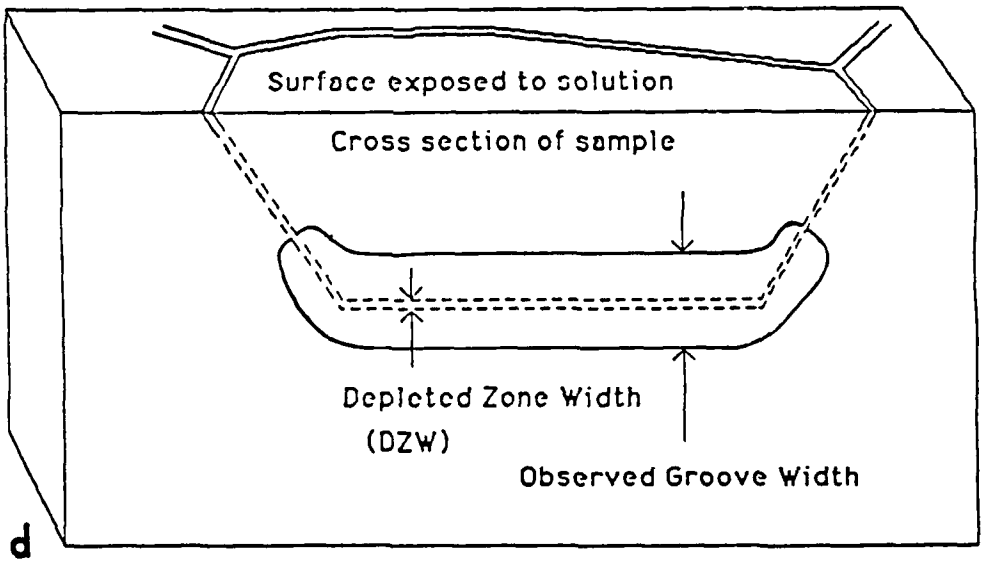
Surface exposed to solution
Cross section of sample
Depleted Zone Width
(DZW)
Observed Groove Width
d

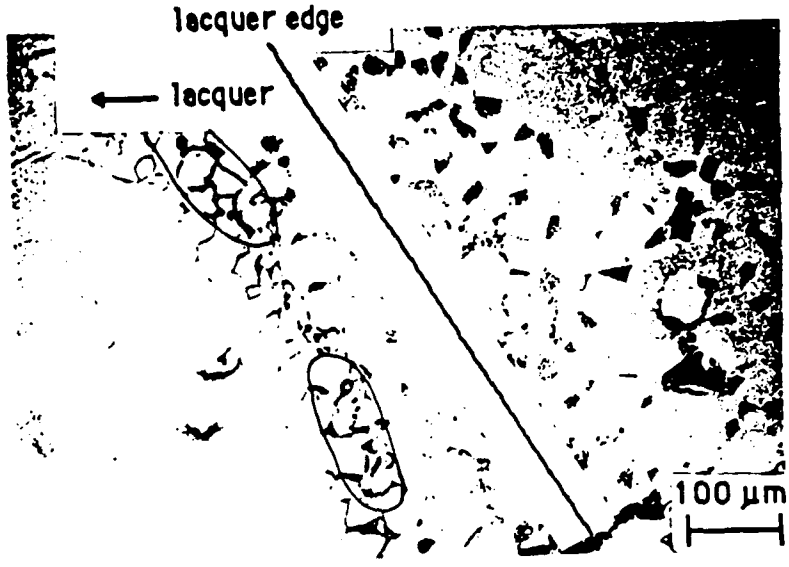
lacquer edge
lacquer
100 µm

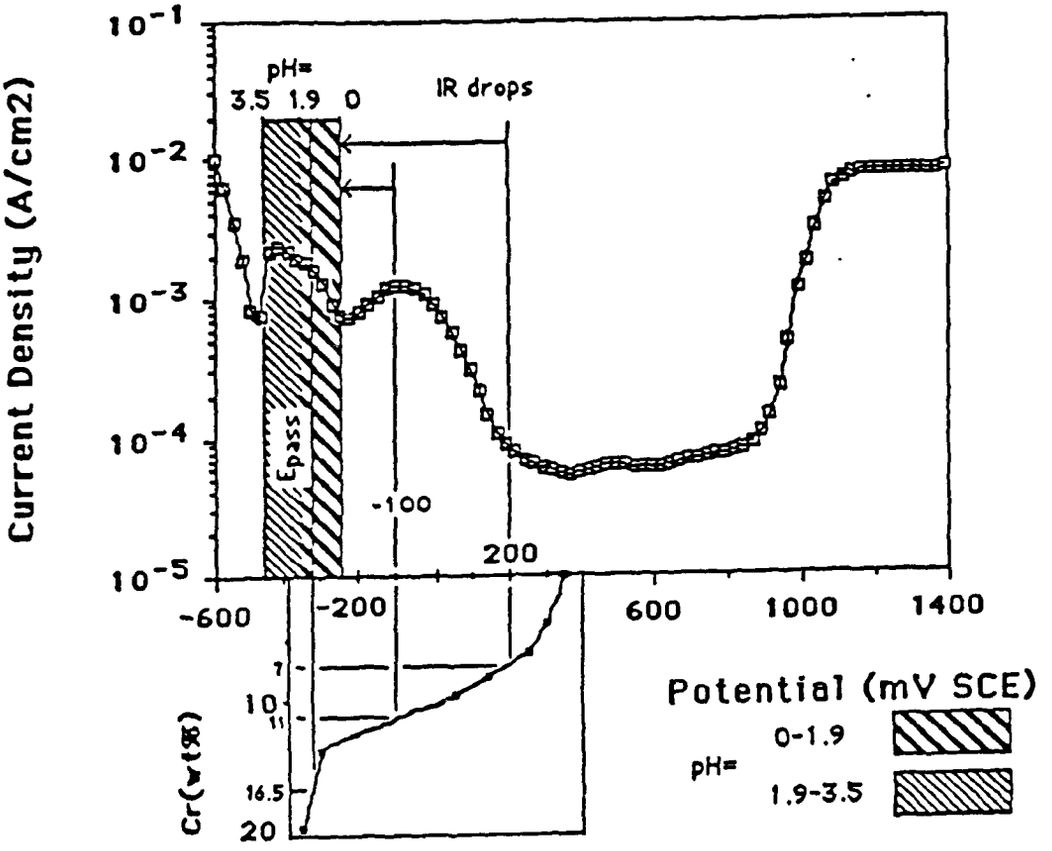

Fig. 7. Kelly, et.al.

DISTRIBUTION LIST

Prof. G. H. Meier
Department of Metallurgical & Mat. Eng.
University of Pittsburgh
Pittsburgh PA 15261

Prof. F. S. Pettit
Department of Metallurgical & Mat. Eng.
University of Pittsburgh
Pittsburgh PA 15261

Prof. Howard W. Pickering
Dept. of Mat. Sci. & Eng.
The Pennsylvania State University
University Park PA 16802

Prof. D. J. Duquette
Dept. of Metallurgical Eng.
Rensselaer Polytechnic Inst.
Troy NY 12181

Prof. D. Tomanek
Dept. of Physics and Astronomy
Michigan State University
East Lansing MI 48824-1116

Dr. M. W. Kendig
Rockwell International Sci. Center
1049 Camino Dos Rios, P. O. Box 1085
Thousand Oaks CA 91360

Prof. R. A. Rapp
Dept. of Met. Eng., 116 West 19th Av
The Ohio State Univesity
Columbus OH 43210-1179

Dr. R. D. Granata
Zettlemoyer Center for Surface Studies
Bethlehem PA 18015

Dr. G. D. Davis
Martin Marietta Laboratories
1450 South Rolling Rd.
Baltimore MD 21227-3898

Dr. S. M. Lipka
Dept. of Ocean Engineering
Florida Atlantic University
Boca Raton FL 33431-0991

Prof. J. Kruger
Dept. of Mat'ls Science & Eng.
The Johns Hopkins University
Baltimore MD 21218

Dr. B. G. Pound
SRI International
333 Ravenswood Ave.
Menlo Park CA 94025

Prof. C. R. Clayton
Dept. of Materials Science & Engineering
State University of New York, Stony Brook
Long Island NY 11794

Dr. J. E. Oldfield
Cortest Laboratories Ltd.
23 Shepherd Street, Sheffield
S3 7BA, ENGLAND

Ms. D. M. Aylor
Code 2813
David Taylor Research Center
Annapolis MD 21402-5067

Prof. G. Simkovich
Dept. of Materials Science & Engineering
The Pennsylvania State University
University Park PA 16802

Dr. P. S. Pao
Code 6303
Naval Research Laboratory
Washington DC 20375

Dr. N. S. Bornstein
United Technologies Research Center
East Hartford CT 06108

Dr. B. A. Shaw
Dept. of Eng. Sci. & Mechanics
228C Hammond Bldg., Penn State University
University Park PA 16802

Prof. R. M. Latanision
Massachusetts Institute of Technology
Room 8-202
Cambridge MA 02139

Dr. R. E. Ricker
National Institute of Standards & Technology
Bldg. 223, Room B-266
Gaithersburg MD 20899

Dr. F. B. Mansfeld
Dept. of Materials Science
University of Southern California, Univ. Park
Los Angeles CA 90889

Dr. W. R. Bitler
115 Steidle Bldg., Dept. of Mat. Sci. & Eng.
The Pennsylvania State University
University Park PA 16802

Dr. S. Smialowska
Dept. of Metallurgical Eng., 116 W. 19th Ave.
The Ohio State University
Columbus OH 43210-1179

Dr. R. V. Sara
Union Carbide Corp., UCAR Carbon Co., Inc.
Parma Technical Center, 12900 Snow Road
Parma OH 44130

Prof. M. E. Orazem
Dept. of Chemical Engineering
University of Florida
Gainesville FL 32611

Prof. J. O'M. Bockris
Dept. of Chemistry
Texas A & M University
College Station TX 77843

Dr. V. S. Agarwala
Code 6062
Naval Air Development Center
Warminster PA 18974-5000

Prof. Harovel G. Wheat
Dept. of Mechanical Engineering
The Univ. of Texas, ETC 11 5.160
Austin TX 78712-1063

Prof. S. C. Dexter
College of Marine Studies
University of Delaware, 700 Pilottown Rd.
Lewes DE 19958

Prof. R. P. Gangloff
Dept. of Mat. Sci. & Eng., Thornton Hall
University of Virginia
Charlottesville VA 22903-2442

Dr. Wayne C. Tucker
Dept. of Ocean Engineering
University of Rhode Island
Kingston RI 02881

Mr. M. M. Opeka
Code K22
Naval Surface Warfare Center
Silver Spring MD 20903-5000

Dr. E. McCafferty
Code 6322
Naval Research Laboratory
Washington DC 20375-5000

Dr. R. L. Jones
Naval Research Lab
Code 6179
Washington DC 20375-5000

Defense Documentation Center
Cameron Station
Alexandria VA 22314 (12)

Office of Naval Research, Dept. of the Navy
800 N. Quincy St.
Arlington VA 22217
ATTN: Code 1131 (3)

Naval Research Laboratory
Washington DC 20375
ATTN: Codes 6000, 6300 and 2627 (3)

Naval Air Development Center
Warminster PA 18974
ATTN: Dr. J. DeLuccia

Commanding Officer
Naval Surface Warfare Center
Silver Spring MD 20903-5000
ATTN: Library and CodeR33 (2)

Naval Ocean Systems Center
San Diego CA 92152-5000
ATTN: Library

Naval Postgraduate School
ATTN: Mechanical Engineering Dept.
Monterey CA 93940

Naval Air Systems Command
Washington DC 20360
ATTN: Codes 310A, 5304B, 931A (3)

Naval Sea Systems Command
Washington DC 20362
ATTN: Codes 05M and 05R (2)

Naval Air Propulsion Center
ATTN: Library
Trenton NJ 08628

Naval Civil Engineering Laboratory
ATTN: Materials Div.
Port Hueneme CA 94043

Naval Electronics Laboratory
San Diego CA 92152
ATTN: Electronic Materials Science Div.

Commander
David Taylor Research Center
Bethesda MD 20084

Naval Underwater System Center
Newport RI 02840
ATTN: Library

Naval Weapons Center
China Lake CA 93555
ATTN: Library

NASA Lewis Research Center
21000 Brookpark Road
Cleveland OH 44135
ATTN: Library

National Institute of Standards & Tech.
ATTN:Met. Div., Cer. Div., Frac. & Def. Div.
Gaithersburg MD 20899
(3)

Office of Naval Research
Ohio State Univ. Res. Ctr., 1960 Kenny Rd.
Columbus OH 43210-1063

Naval Facilities Engineering Command
Alexandria VA 22331
ATTN: Code 03

Commandant of the Marine Corps
Scientific Advisor
Washington DC 20380
ATTN: Code AX

Army Research Office
P. O. Box 12211
Research Triangle Park NC 27709
ATTN: Met. & Cer. Pro.

Army Materials Technology Laboratory
Watertown MA 02172-0001
ATTN: Res. Pro. Off. (1)

Air Force of Scientific Research
Building 410, Bolling Air Force Base
Washington DC 20332
ATTN: Elec. & Mat. Sci.

NASA Headquarters
Washington DC 20546
ATTN: Code RM

Oak Ridge National Laboratory
P. O. Box X
Oak Ridge TN 37380

Los Alamos Scientific Lab.
P. O. Box 1663
Los Alamos NM 87544
ATTN: Rept. Librarian

Argonne National Laboratory
Metallurgy Division, P. O. Box 229
Lemont IL 60439

Brookhaven National Laboratory
Technical Information Div., Upton Long Island
New York NY 11973
ATTN: Research Library

Lawrence Berkeley Laboratory
1 Cyclotron Road
Berkeley CA 94720
ATTN: Library

David Taylor Research Center
Annapolis MD 21402-5067
ATTN: Codes 281, 2813 and 0115 (3)

Prof. H. K. Birnbaum
Dept. of Metallurgy & Ming. Eng.
University of Illinois
Urbana IL 61801

DOD Metals Information Analysis Ctr. (MIAC)
CINDAS/Purdue University
West Lafayette IN 47906-1398